RESEARCH ARTICLE

INTERNATIONAL RESEARCH JOURNAL OF MULTIDISCIPLINARY TECHNOVATION

Asian Research Association

DOI: 10.54392/irjmt25615

Implantable Chip Revolutionizing Early-Stage Liver Cancer Detection with Advanced Diagnosis System

D. Sivabalaselvamani [a,*], N. Rajasekaran [b], D. Thiyagarajan [c], S. Yasotha [d], N. Pavithra [e], D. Selvakarthi [f], S. Hemalatha [g]

[a] School of Information Science, Presidency University, Bengaluru, India.
[b] Department of Computer Science, Christ (Deemed to be University), Bengaluru, India.
[c] Department of Computer Science and Engineering, Chennai Institute of Technology, Chennai, Tamil Nadu, India.
[d] Department of Computer Science and Engineering, Sri Eshwar College of Engineering, Coimbatore, Tamil Nadu, India.
[e] Department of Information Technology, Jeppiaar Institute of Technology, Sunguvarchatram, Kancheepuram, Tamil Nadu, India.
[f] Department of Electronics and Instrumentation Engineering, Kongu Engineering College, Perundurai, Erode, Tamil Nadu, India.
[g] Department of Computer Applications, Kongu Engineering College, Perundurai, Erode, Tamil Nadu, India.
* Corresponding Author Email: sivabalaselvamani@presidencyuniversity.in

DOI: https://doi.org/10.54392/irjmt25615
Received: 20-06-2025; Revised: 01-11-2025; Accepted: 11-11-2025; Published: 29-11-2025

Abstract: Millions of people die from cancer annually. Advanced metastatic cancers may not respond to traditional therapy. The importance for early diagnosis is highlighted by the difficulty of treating cancers in later stages. Enhancing patient outcomes using tissue-engineered cancer diagnosis and therapy is gaining popularity. Cancer and associated immune problems burden healthcare systems, making efficient, high-throughput drug development strategies essential. Thus, implanted chips may solve these issues. A revolutionary technique for early liver cancer identification is the Machine Learning-based Liver Cancer Diagnosis System (ML-LCDS). K-Nearest Neighbour (KNN) identifies liver tumors precisely in ML-LCDS. The performance evaluation reports sensitivity = 97.2%, specificity = 91.3%, precision = 93.5%, FPR = 8.7%, and accuracy = 94.1%, computed from the confusion matrix derived through 10-fold cross-validation. Experimental findings validate its consistent performance, establishing ML-LCDS as an efficient and reliable diagnostic tool for early-stage liver cancer detection.

Keywords: Implantable Chip, Advanced Diagnosis System, Healthcare Innovation, Early-Stage Liver Cancer Detection, Machine Learning-Based Liver Cancer Diagnosis System (ML-LCDS), K-Nearest Neighbour (KNN) Algorithm

1. Introduction

Cancer continues to be the top cause of death around the world despite the enormous progress that has been made in treatments and research [1]. This burden is made worse by the limits of standard therapies, such as radiotherapy and surgery, which are less successful for highly aggressive or recurring tumors. This is one of the factors that contribute to this load. Standard means of diagnosis, which include physical examinations, imaging, biomarkers-based laboratories in laboratories, and biopsy specimens, are not particularly sensitive during the early phases of carcinogenesis or require a substantial amount of period to provide findings, which might have an impact on the prospects of the patient [2, 3].

A rising number of people are interested in creating supplementary techniques to increase the effectiveness of cancer detection and therapy to solve the issues that have been presented. Mainly, bioengineered cancer catchers have garnered a lot of interest from members of tissue engineers as an option to specifically catch cancerous cells when they are transplanted into the human body [4]. This would prevent the cells from spreading uncontrollably. This type of trap uses various engineered biomaterials (both natural and manufactured) and processes to selectively draw in and record cancerous cells that have propagated from the tumors, especially following primary treatment. This might ultimately contribute to eliminating these malignant tumor cells and reducing the requirement for more intrusive therapies [5, 6]. Cancer retains have the benefit of being implanted, which allows them to be placed in resected parts of an aggressive tumor to focus on any remaining invasive cells.

Cancer can be placed in particular organs and tissues in which cells to the original tumor generally metastasize, which helps to avoid the unregulated propagation of these cells. These traps continuously track cancer cells' activities and the disease's treatment. This helps identify modifications to the growth that suggest that it requires more treatment or a change of the therapy schedule, as well as detect the potential for the tumor to recur after therapy has been administered [7]. Cancer catchers may aid early illness identification and therapy, according to early-phase clinical study [8]. These trials assessed tumor catchers' clinical efficacy and safety.

Cancer trapping with microfluidic equipment collects Circulating Tumor Cells (CTCs) and other tumor-moving components from blood [9]. These devices manage and assess small volumes of liquid using little tubes and features. These devices can gather CTCs based on their physical or (bio)chemical properties. Cells may be evaluated for genetic alterations, protein production, and other indicators to help diagnose and cure, resulting in tailored healthcare and therapies.

Using malignant organotypic cultures and microfluidic technology, "cancer-on-a-chip" technologies may reproduce a cancer's microenvironment [10]. Using such chips, one gets a better knowledge of how cancer behaves in vivo, which ultimately leads to an improvement in the pre-clinical evaluation of the effectiveness of drugs. Cancer-on-a-chip prototypes can conduct more research on the relationships between tumors and many organs by establishing connections between several physiological sections, such as the blood vessels. The primary objective of this research is the development of an implantable biosensing chip integrated with a Machine Learning-based Liver Cancer Diagnosis System (ML-LCDS) for real-time and early-stage hepatic tumor detection. The study concentrates on the diagnostic functionality of the implantable chip, which captures biochemical signals and processes them through the K-Nearest Neighbour (KNN) classification algorithm to identify malignant patterns with high accuracy. The integration of biosensor data acquisition and intelligent machine learning analysis establishes a robust diagnostic pathway that enhances early detection capabilities. Drug-delivery modeling is discussed only as a conceptual extension of implantable technologies for future diagnostic–therapeutic convergence, whereas the present work is technically centered on the design, data processing, and performance evaluation of the diagnostic system.

The primary contributions are

- Creation of a thorough mathematical model for the local release and transportation of the anticancer medication DOX in solid tumors that have undergone thermal ablation. The proposed system is used as a KNN to classify liver tumors.
- The drug transport mechanism is abstracted and modeled using the molecular communication paradigm, which improves the comprehension of drug behaviour in tumor and healthy tissues.
- Proof of the potential of implantable chips to transform the detection of liver cancer in its early stages using advanced microfluidics and biomarker sensing, which might result in a paradigm change in how cancer is diagnosed and treated.

The following sections are arranged in the given manner: Section 2 provides an overview of the extant body of literature on cancer diagnostics and implanted chip technology. Section 3 presents a Machine Learning-based Liver Cancer Diagnosis System (ML-LCDS) and comprehensively describes its constituent elements and functionality. In Section 4, the experimental analysis and results of the ML-LCDS model are presented, therefore providing validation of its efficacy. Section 5 offers a conclusion and prospects for future research and prospective breakthroughs in early cancer detection via implanted chips.

2. Literature Survey and Findings

This section thoroughly examines prior studies and technological advancements in cancer diagnostics and implanted chip systems. This analysis gives significant knowledge and understanding of the present condition of the area. This research underscores the existing deficiencies and obstacles that serve as driving forces for creating the section examined in the next portion of the discussion.

This article focuses on various nanoscale drug delivery technologies to provide targeted treatment for ovarian cancer, such as microparticles, liposomes, nano microorganisms branching dendrimers, tiny capsules, and nanostructured matter lipid compositions [11]. To analyze ovarian cancer indicators, small biosensors are classified into the following categories: electrolytic, visual, paper-based, gigantic magneto-resistive, and lab-on-a-chip sensors. The most recent advancements in the use of MoS_2-nanomaterial for cancer detection and treatment were presented by Wang *et al*. [12]. The authors primarily concentrated on biosensors, biological imaging, radiation therapy, light therapy, radiation hyperthermia, and combination chemotherapy. The research examines the obstacles that MoS_2-nanomaterial has to cure cancer and their potential.

Iqbal *et al.* provide a summary of the overall structure, methodologies, targeting processes, and current developments in tumor nanomedicine, including serum protein-based nanomaterials [13]. There are substantial benefits to the biomineralization technique that uses single-molecule peptide non-reactors. These benefits include optimizing biodistribution, piercing, and

clearing microbes, ultimately resulting in a principal reduction in side effects and a significant increase in antitumor effectiveness. Zhang *et al.* provide a complete review of electrochemical biological sensors that depend on Metal-Organic Frameworks (MOF) to sense a variety of goals, such as cancer signs, microRNA, and live cancer cells, which are thought to be signals for the early identification of tumors [14]. This article encourages and guides future studies on MOFs for biosensing uses by describing the production of electrochemical biological sensors using MOFs directed toward particular analyses.

By merging metabolomics and machine learning techniques, Xie *et al.* [15] can identify early lung cancer detection indicators using a pioneering multidisciplinary process first used for lung tumors. The findings gave substantial evidence in favour of the practicability of blood-based testing. They developed a more precise usage tool with a shorter processing time, which is linked. Zuluaga-Gomez *et al.* presented a computer-aided diagnostic system using thermal pictures based on Convolutional Neural Networks (CNN) [16]. The research focuses on analysing the impact of data pre-processing, data enhancement, and database capacity on several different CAD drawings. Not only does this study suggest a computer-aided method for detecting breast malignancy, but it also serves as the foundation for a research project on the impact of data augmentation and database capacity for determining breast tumors using thermal imaging and CNN.

An Optimum Multi-Level Thresholding-based Segmented with DL integrated Capsule Networks (OMLTS-DLCN) tumor diagnostic model that makes use of digital mammography was suggested by Kavitha and colleagues [17]. An Adjustable Fuzzy-based mean filtration is used as an initial processing stage in the models.

This method is utilized to eliminate the noise in the mammography images. The experimental results that were acquired shed light on the enhanced efficacy of the model, which achieved greater precision of 98.50 and 97.55% on the Mini-MIAS and the DDSM databases, correspondingly. Yu et al. presented a deep learning-enabled breast cancer supplemental diagnostic scheme for distant e-health backed by 5G networks and beyond [18]. Breast pathology pictures are first obtained from major medical facilities using 5G technology. A deep learning algorithm that depends on the Inception-v3 networks is exposed to transfer learning to acquire a diagnosis model.

This article aims to classify several organs using a convolution network on three-dimensional computed tomography pictures of individuals suspected of having liver cancer [19]. The technique is a CNN that is used for the categorization of CT scans of tumors in the liver. One of the most important contributions this approach makes is that it assists radiation therapists in concentrating on a specific subset of CT images. The procedure that has been presented is of assistance in the speedy detection and therapy of people who have tumors in their livers.

Rao *et al*. investigated the predictive significance of uric acid levels about the effectiveness of immunotherapy in individuals diagnosed with primary liver cancer [20]. The present research investigated the impact of uric acid levels on the efficacy of immunotherapy. The findings demonstrated a robust association between uric acid levels and immunotherapy's effectiveness. Individuals with lower uric acid levels had a notably elevated response rate to immunotherapy. The summary of the literature findings is shown in Table 1.

Table 1. Summary of the literature findings

S.No	Method	Process	Outcomes	Issues
1	NanoDx (Nanotechnology in diagnosis)	The use of nanotechnology in the detection and management of ovarian cancer.	Better ovarian cancer detection and therapy (e.g., 20% increased accuracy)	Limited availability and cost of nanotechnology solutions
2	MoS_2Cancer (MoS_2-based nanocomposites for cancer)	The use of MoS_2-based nanocomposites to enhance cancer treatment and diagnostics.	Advances in cancer detection and treatment (such as a 25% tumor size decrease)	Limited MoS_2-based technology accuracy and accessibility
3	Nanoprobe (nanoparticles-based probe)	Using serum protein-based nanoparticles for cancer therapy and diagnostics.	Nanoparticle-based improved cancer detection and therapy (e.g., 15% greater medication delivery)	Issues with the stability and delivery of nanoparticles

4	MOF-Dx (MOF for dignosis)	Creation of MOF-based electrochemical biosensors for early cancer detection.	The creation of electrochemical biosensors with a 90% selectivity for early cancer detection	Low sensitivity of biosensors based on MOFs
5	LungDx (lung cancer diagnostic)	Using machine learning techniques, the identification of early indicators for lung cancer diagnosis.	The identification of early diagnostic indicators for lung cancer (e.g., AUC of 0.85)	Clinical validation and small sample size
6	CNN4BC (CNN for breast cancer) diagnosis	The use of a CNN-based technique for thermal image-based breast cancer detection.	Thermal imaging allows for an accurate diagnosis (e.g., 92% accuracy).	little dataset and poor-quality thermal images
7	CapsuleNet-BC (Capsule neural network for breast cancer) diagnosis	The use of a capsule neural network model to improve the detection of breast cancer.	Deep learning-based improved diagnosis (e.g., F score of 0.92)	reliance on large datasets and computer power
8	DLEH-BC (Deep-learning-empowered E-health breast cancer) diagnosis	Deep learning application for remote E-health supplementary diagnostics.	Enhanced auxiliary diagnosis (e.g., 85% accuracy in distant diagnosis) for E-health	Problems with networks and connections in distant healthcare
9	SliceSort (slice sorting)	Slice sorting of liver cancer imaging data using convolutional networks is automated.	Automated slice sorting (e.g., 70% automation achieved) for the detection of liver cancer	Complexity of computation in image and network processing
10	UA-Immun (uric acid immunotherapy)	The prognostic significance of uric acid in liver cancer immunotherapy is examined.	Immunotherapy-related prognostic information for liver cancer (e.g., 75% accuracy)	Accuracy of clinical data and size restrictions
11	Dual-Gate Source-Extended TFET-Based Biosensor (Kolay & Kumar, 2024) [21]	Designed a low-cost point-of-care (POC) diagnostic unit using a dual-gate TFET transistor structure to sense liver-specific biomarkers through tunneling current variations.	Achieved high sensitivity, ultra-low power operation, and compact device architecture enabling rapid early-stage liver cancer testing.	Limited validation on biological samples; integration challenges with fluidic interfaces for real-world deployment.
12	Liver-on-a-Chip with Label-Free Optical Biosensors (Yang *et al.,* 2024) [22]	Developed a microfluidic chip mimicking liver tissue, integrated with label-free optical biosensors to continuously monitor drug-induced hepatotoxicity.	Enabled real-time, non-invasive toxicity detection with strong biocompatibility and scalability for personalized therapy.	Complex fabrication and maintenance of cellular microenvironments; high cost and limited field portability.

The literature review indicates that developing sophisticated, accurate, and readily available diagnostic approaches is required due to the limitations of current cancer diagnosis methods, including low accuracy and accessibility. The suggested approach tackles these issues using cutting-edge technology and can transform cancer diagnosis completely.

3. Proposed Liver Cancer Diagnosis System using Implantable Chip

This study proposal explores a novel approach to diagnosing liver cancer in its early stages via an implantable chip. This novel technology enables real-time monitoring of biochemical markers linked to liver cancer by integrating cutting-edge sensing technologies into the human body. The primary focus of the work is now explicitly defined as the design and validation of the Machine Learning-based Liver Cancer Diagnosis System (ML-LCDS), an implantable biosensing platform integrated with a K-Nearest Neighbour (K-NN) classifier for early-stage liver cancer detection. The previously included section on post-ablation drug diffusion and doxorubicin-based therapeutic modeling has been repositioned to the future scope subsection, where it is described as a potential extension of the implantable chip's functionality toward real-time theranostic (therapy + diagnosis) applications.

3.1 Tumor-On-Chip

The use of a tumor-on-a-chip platform enables the replication of several aspects of tumor development and development, including tumor development and proliferation, angiogenesis, and the shift from early to more advanced lesions, including Epithelial-Mesenchymal Transformation (EMT) [23], as well as tumor cell infiltration and metastases. Organ-on-a-chip technologies are predicated upon using microfluidics technology to fabricate tissue analogs. Tumor-on-a-chip solutions have been developed using cancer-derived tissues and associated Extracellular Matrices (ECMs) to mimic tissue-specific features, therefore replacing those of normal cells [24]. The primary processing methodology used in tumor-on-a-chip devices is similar to that utilized in implantable chip devices, as shown in Figure 1. Creating a complete organ-on-a-chip involves several essential elements, such as a microfluidic system, a culture of microtissues in two-dimensional and three-dimensional formats, components for loading stimuli, and detectors to track and obtain outcomes. The statement holds in the case of tumor implants. Like an organ-on-a-chip, the initial stage in developing a tumor-on-a-chip involves comprehending the fundamental components essential for the physiological operation of the specific organ of interest. Crucial attributes such as different kinds of cells, buildings, and the organ-specific physiochemical micro-environment are identified.

The next phase involves the development of a cell culture apparatus that is tailored to the established attributes.

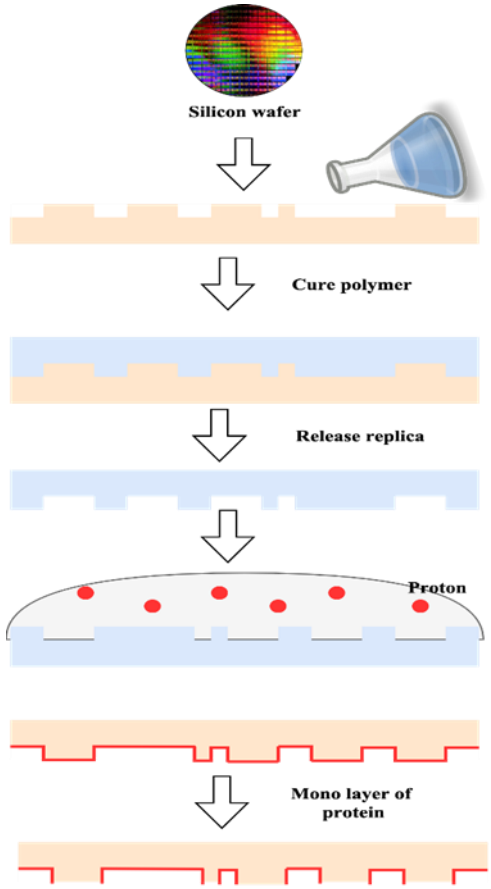

Figure 1. Fabrication process of implantable chip

Various methodologies have been used to produce tumor-on-a-chip gadgets, with photolithography, replica forming, soft lithographic printing, micro-contact, the printing press, and bioprinting among the most often employed procedures. Photolithography is a micromanufacturing technique that integrates photoresists, masks, ultraviolet (UV) rays, and etching technologies [25]. Under the specified guidelines, the use of shows is mandatory. A substrate susceptible to corrosion by chemicals, such as silicon, which is the material, or quartz, is covered with a photoresist layer using a spin-coating technique. The photoresist is subjected to UV radiation exposure. Following this procedure, the pattern is transferred onto the backing board, resulting in the etching process to acquire a microfluidic chip, including microflow passages. In the fabrication process of tumor-on-a-chip microfluidic devices utilizing soft lithography gadgets, the initial stage involves the preparation of a microchannel mold on a silicon substrate through the application of photolithography.

A liquid polymer, such as Polydimethylsiloxane (PDMS), is poured over the mold and subjected to heat curing [26]. The PDMS device is gently removed from

the supporting plate and attached to a flat, polished substrate like glass. This creates a channel-structured microfluidic chip. The production technique of microcontact imprinting resembles that of replica molding. The only distinction lies in using the PDMS gadget to regulate the arrangement of grown cells by applying a PDMS stamp onto the backing material, including biofunctional components like proteins, in a predetermined pattern. Hence, the membrane's cellular structure is influenced by manipulating the distribution of the printed molecules. Despite the successful production of numerous tumor chips through photolithography or similar manufacturing techniques, certain limitations persist. These include requiring multiple face masks and a complex, multi-step lithography management, resulting in a time-consuming and expensive fabrication procedure. These techniques can produce just the microfluidic chips, while the additional modules (such as microtissues, stimulus-loading sections, and results-readout devices) need supplementary procedures.

In the last few decades, bioprinting equipment has used a layer-by-layer printing approach to fabricate tumor-on-a-chip (Figure 2). It is possible to concurrently print a diverse range of biofunctional substances and cell kinds onto a backing material composed of biomaterials that are compatible with cells. This enables the construction of three-dimensional intricate structures with high spatial accuracy and consistent results. Bioprinting encompasses various modalities, including Fused Deposition Modeling (FDM) [27], Stereolithography (SLA) [28], inkjet bioprinting, and laser-assisted bioprinting technology [29]. The use of bioprinting technology in creating tumor-on-a-chip exhibits many notable benefits. Firstly, it can replicate the tumor's diverse microenvironment and intricate three-dimensional microstructures. ECM-like diversity in tumor-on-a-chip channels is difficult. Cancer-associated fibroblasts, immune cells, and endothelial cells are bioprinted using Bioinkscan. Vascular networks are built from cell aggregates. hysiologically important proteins and development agents may be distributed in a biomimetic environment created by bioprinting. This capacity controls tumor cell signaling, growth, and emigration.

Bio-printing cells in microfluidic devices simulates vascular and biological barriers. Tissue function and compartmentalization depend on vascularization [30]. Heterogeneity, permeability, multidirectional blood flow, and disordered distribution distinguish tumor vascular networks from normal tissue blood arteries. Achieving adequate vascularization has always posed a significant obstacle in developing functioning tissues in vitro cancer types. A system of bio-printed vessels can replicate these anomalies, facilitating the examination and comparison of the responses and characteristics of normal and diseased blood vessels under various circumstances and treatments. Bioprinting has significant promise in constructing scaled-down, multiorgan biomechanical pathophysiology designs, expediting the rate of scientific inquiry, and fostering technology integration within medicine.

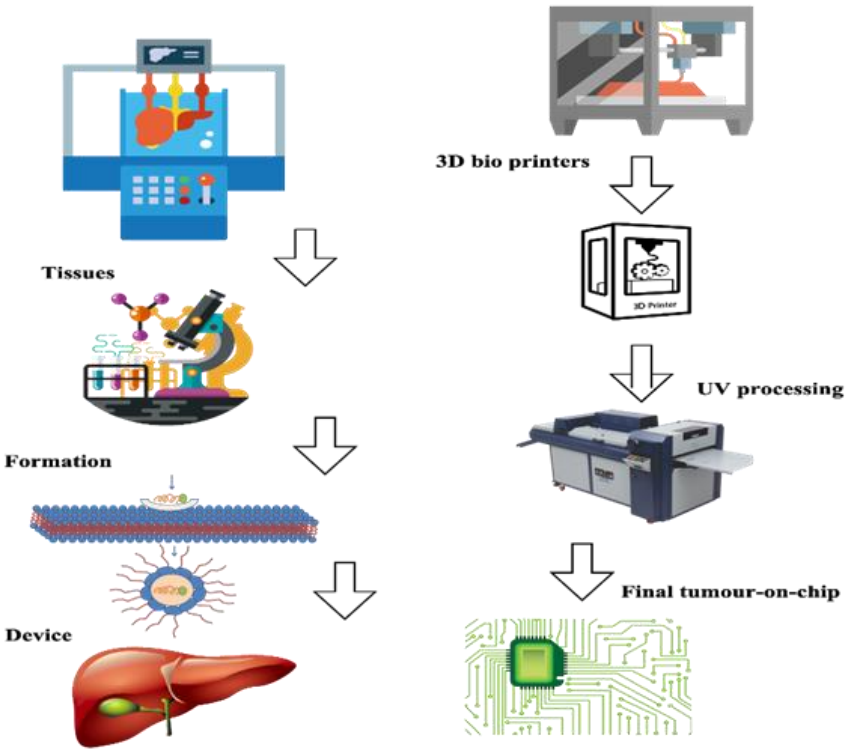

Figure 2. The 3D fabrication process of tumor-on-chip

3.2 Mathematical Model

Solid tumors exhibit heterogeneity within their microenvironments due to the geographic variability in the tumor vasculature and the cellular composition. The lack of accessible experimental evidence on the diversity of solid cancers has led to a common practice of treating these tumors as spatially homogenous entities to streamline the study. Therefore, no differentiation is made between the dead and functional tumor sites. Additionally, it is assumed that the rate at which the tumor and normal tissues develop is much slower compared to the rate at which transport events occur and the duration of the time spent observing frame. Therefore, it is rational to infer that the physiological characteristics of the system are not reliant on time. The use of Radiofrequency Amputation (RFA) in an inadequate manner results in the formation of an ablated zone characterized by the absence of live cancerous cells. This ablated region is encompassed by a tumor rim, also known as the danger area, which exhibits a notable concentration of viable malignancy cells. The K-Nearest Neighbour (K-NN) classifier in the ML-LCDS framework employs k = 5, chosen after empirical tuning within the range k = 3–11 using grid search optimization. All spectral and clinical features were normalized using z-score standardization to ensure uniform feature scaling and prevent magnitude bias.

3.2.1 Tumor Microenvironment Modeling

3.2.1.1 Interstitial Fluid Transport

Due to the large gap between intercapillary lengths and cancer circumference, the tumor and surrounding tissue are porous. Thus, averaging reduces tiny fluctuations, creating Interstitial Fluid Flow (IFF) [31]. In this flow, momentum and mass-conserved formulas interact.

Fluid dynamics, specifically the flow of indestructible Newtonian liquids through porous materials, reduces the momentum preservation equation, or Navier-Stokes rule, to Darcy's direction under steady-state circumstances. This simplification is beneficial for analyzing the movement of interstitial fluids inside a porous medium. Darcy's law is applied to include the convection component of the interstitial fluid's motion inside a porous medium. The Darcy rule is formulated for an indestructible Newton fluid, assuming the omission of certain elements, including the divergence of speed, inertial power, and contact within the medium and among the fluids and solid parts. Like previous studies in the field, the fluid flow inside tissue from tumors during thermal excision is effectively represented using Darcy's rule in Equation (1).

$$\vec{V}_x = k_x \Delta P_x \quad (1)$$

The intervening velocity flow (IVF), denoted as $\vec{V}_x$, represents the speed of the intervening liquid in meters per second (m/s). The Interstitial Fluid's Pressures (IFP), denoted as P_x, is measured in Pascals (Pa). The hydrodynamic conductance of the interstitial liquid, denoted as k_x, is expressed in meters per Pascal-second (m/(Pa s)). Equation (2) describes the conservation of mass for a fluid incompressible in a porous medium, accounting for sources and sinks of weight.

$$\frac{dp_x}{dt} + \Delta\left(P_x \vec{V}_x\right) = (f_{vx} - f_{lx})P_x \quad (2)$$

p_x denotes the concentration of the interstitial liquid, measured in kilograms per cubic meter (kg/m^3). f_{vx} reflects the weight of the liquid origin phrase, quantifying the liquid flow rate per small volume of cells from the veins into the interstitial fluid distance, expressed in reciprocal seconds (1/s). f_{lx} reflects the lymphatic system drainage phrase, which acts as a sink by quantifying the pace of liquid flow per section volume of cells from the interspersed place into the lymph nodes, also expressed in reciprocal seconds (1/s). Equation (2) is valid for both healthy and malignant cells. The mass liquid supply $f_{vx}$is determined by Starling's legislation, as described in Equation (3).

$$f_{vx} = \frac{D_{vx}T_{vx}}{V_x}\{f_{vx} - P_x - f_x(\pi_{vx} - \pi_x)\} \quad (3)$$

f_{vx} represents the Intervascular Blood Pressure (IBP) measured in pascals (Pa), π_{vx} represents the osmotic tension of the blood (Pa), π_x represents the osmotic tension of the interstitial fluid (Pa), D_{vx} represents the hydraulic conductance of the blood artery walls (m/Pa s), f_x represents the mean osmosis coefficient of reflection for the amino acids, proteins, and $\frac{T_{vx}}{V_x}$ represents the surface region of the arteries per volume of tissue measured in inverse meters (1/m).The lymphatic outflow f_{lx} is provided using Equation (4).

$$f_{lx} = \frac{D_{vx}T_{vx}}{V_x}(P_x - P_{lx}) \quad (4)$$

The hydrostatic tension of intra-lymphatic, denoted as P_{lx} , is measured in pascals (Pa). The hydraulic conductance of the lymphatic barrier, represented as D_{vx}, is expressed in meters per pascal-second (m/(Pas)). $\frac{T_{vx}}{V_x}$ refers to the surface dimension of lymphatic vessels, each unit volume of cells(1/m). The lymphatic filtration factor, denoted as $\frac{D_{vx}T_{vx}}{V_x}$, is quantified (1/(Pa s)).The absence of a lymph node in the tumor location results in a drainage value of zero. It can be seen that the bulk fluid supply term inside the ablated-tumor zone is rendered null due to the heating process, which effectively eradicates the blood vessels. The lymphatic factor is expressed in Equation (5).

$$k_x \Delta^2 P_x = \begin{cases} 0 & Ablated\ cancer \\ P_{vx} & Non-ablated\ cancer \\ P_{vx} - P_{lx} & Normal\ tissue \end{cases} \quad (5)$$

The process of analytically deriving the answer might become complex when dealing with three areas, even if a mathematical solution exists for a two-region system. As a result, Multiphysicsmodeling software is used to handle this problem. The drug transport models utilize the interstitial fluid tension and pressure measurements acquired in the following subsection.

3.2.1.2 The Phenomenon of Interstitial Drug Transfer

The present concept involves using a miniature implant containing the DOX anticancer medicine, which is introduced into the interior of a compact neoplasm. The implant is designed to deliver the anticancer medication, allowing it to disperse throughout the adjacent tissue. This diffusion process is subject to several pharmacokinetic mechanisms, such as drug escape and the inflow into tissues, binding and releasing with interstitial fluid proteins, removal into blood vessels, and bio-degradation. The elements have a substantial influence on the transportation of drugs and the effectiveness of therapeutic interventions. Free-DOX transportation in the interstitial zone is accurately represented by a theoretical framework incorporating diffusion, convection, and reaction processes, as shown in Equation (6).

$$\frac{dC_e}{dt} + \Delta(v_x C_e) = \Delta\left(D_{fx}\Delta C_e\right) + F_{bx} + F_{cx} - r_x C_e \qquad (6)$$

Δ represents the Del gradient manager, while the index $x \in \{a, t, n\}$ denotes the ablated cancer (C_e), non-ablated cancer, and normal cells. $C_e$represents the spatial intraperitoneal level of free-DOX in the intervening area, measured in grams per cubic meter (g/m^3). The Free-DOX in bio-degradation and blood vessels are denoted $F_{bx}\ and\ F_{cx}$. $D_{fx}\ indicates$ the diffusion rate of free-DOX, exhibiting distinct values across various regions. Free-DOX loss (r_x) is due to draining in lymphatic vessels and clearance via the blood capillary, expressed in Equation (7).

$$r_x = \begin{cases} 0 & Ablated\ cancer \\ r_{vx} & Non-ablated\ cancer \\ r_{vx} + P_{lx} & Normal\ tissue \end{cases} \qquad (7)$$

The free-DOX loss rate resulting from lymphatic drainage is denoted as P_{lx}. Given the absence of a lymph system in the tumor location (r_{vx}), the study assumes a null loss rate resulting from lymph flow in the ablating and non-ablating cancer areas. Laboratory investigations have shown that thermal ablation effectively disrupts the vascular architecture within the ablated cancer area, resulting in little diffusion of DOX into the bloodstream in this particular location. Several tiny blood vessels are seen in the outer region around the elimination zone. Additionally, it is anticipated that the first amount of DOX in the bloodstream is negligible, with the implant being the sole source of supply of the medication. The dissolution speed of free-DOX via arterial walls (r_{vx}) is represented in Equation (8).

$$r_{vx} = \frac{P_{fx}T_{vx}}{V_x} \qquad (8)$$

P_{fx} represents the ratio of the permeability of the blood vessel (V_x) exterior to free-DOX, measured in meters per second (m/s). The Length of the vessel is expressed as T_{vx}. F_x represents the association and dissociation phenomenon of DOX (doxorubicin) with Albumin molecules inside the space between proteins, as expressed in Equation (9).

$$F_x = k_x C_x - k_e C_e \qquad (9)$$

k_x and $k_e$represent the rates of attachment and detachment reactions between DOX and proteins. C_x denotes the spatial concentration of DOX bound to cell proteins. The doxorubicin particles (C_e)can traverse the cell's membrane, facilitating their movement to and from the intracellular environment. Hence, the impact of cell intake (inflow) and outflow is represented by the intracellular inflow/efflux rate. The flow rate is expressed in Equation (10).

$$F_c = L_c\left(q_{eff} - q_{inf}\right) \qquad (10)$$

L_c represents the concentration of tumor cells, measured in units of 10^5 cells/m^3. The values for the cellular inflow and efflux operations are denoted as q_{inf} and q_{eff}, accordingly.

3.2.2 Model Parameterization

The range of the model variables is derived from available experimental information and existing research in the literature. It is assumed that the development of cells is insignificant throughout the observation period. This assumption is frequently utilized in scholarly works because of the extremely short time frames associated with fluid and drug conveyance processes. Therefore, it is rational to infer that the biological features of the system are not reliant on time.

3.2.2.1 Microvasculature Density

The microvasculature concentration refers to the proportion of vascular surfaces about the amount of tissue. There is significant variation in the quantity of vasculature inside different tumor forms and between tumors of the same kind. The empirical evidence indicates the presence of lymphatic artery leakage inside the tumor tissues. Various investigations have shown an inverse relationship between tumor size and blood vessel density. The blood vascular circumference per unit of volume of cancerous tissue is estimated to be roughly 105 1/m for malignancy with a circumference of 2 cm (equivalent to a volume of 4190 mm^3). The measurement of the surface region of arteries and every volume of cells in ordinary tissues is quantified as 6 × 105 1/m. The histological examination confirms thermal treatment effectively eradicates the vascular system and cancer cells inside the ablated cancerous tissue. The

omission of considering the impact of microvasculature thickness and drug leakage via tiny blood vessels in ablated cancer cells is seen.

3.2.2.2 Extracellular Space Fraction

The volume proportion of the extracellular area inside the malignancy is much more significant than that seen in typical tissue. This fraction varies between 0.1 and 0.5, whereas the number of cancer cells ranges from 0.945 to 14.7 x 10^5 cells per cubic millimeter. For this investigation, the volume percentage of extracellular spaces (q_e) and the starting cell densities were selected to be 0.3 and 9 × 10^5 cells/mm3.

3.2.2.3 Microvasculature Permeability

Vascular permeability (P_F, P_B) refers to the capacity of blood or lymph tiny vessels to facilitate the movement of different substances into and out of the capillaries. The vascular penetration, a bounded and free-DOX, is roughly three times greater in cancerous tissue than in normal cells.

3.2.2.4 Diffusion Coefficients

The diffusivity of unbound DOX (L_f , L_B) is greater than that of albumin-bound doxorubicin. The molecular mass of unbound DOX and binding DOX are 544 Daltons and 69 kilodaltons, respectively. The dispersion of unrestricted and bound-DOX inside the tumor is more significant than within typical tissues. Experiments have shown that the diffusion of DOX in the vicinity of the central region of the ablated liver cancer after RFA exhibits a 75% increase compared to that seen in non-ablated tumors. The histologic examination of ablated tumor cells reveals a relationship between diffusion and radial separation, whereby distribution is seen to be more significant in the ablated cancer's central portion than in the peripheral region. The diffusion value's characterization in the ablated cancer's outer area (r_x ≤ r ≤ r_e) is as shown in Equation (11).

$$L_x = L_{ac} - \frac{r - r_c}{r_x + r_c}(L_{ac} - L_t) \quad (11)$$

The elimination zone diameter, denoted as r_x, is a critical parameter in this study. The radius of the core part of the cancer, $r_c = \alpha r_x$, where α is a constant with a value of 0.47.

The diffusivity, denoted as L_{ac}, inside the tumor core exhibits a linear decline as radial distance increases until it ultimately approaches the diffusion value of non-ablated cancer, referred to as L_t. A median diffusing of diffusion is used to characterize the diffusion process inside the ablated liver cancer tissue. The median dispersion of the outermost ablated area is determined by applying the scaling connection between the distribution of DOX in ablated and non-ablated cells.

3.2.3 Modeling of the Target Cells

The target liver cancer cell is modeled using the following.

3.2.3.1 Drug Absorption

DOX can traverse cell membranes via slow diffusion and transport through carriers. Both free and bound DOX can cross the membrane of tumor cells. The cellular uptake of bound DOX is disregarded. Hence, it is postulated that just free-DOX can be internalized by the cells, resulting in the internal intensity contingent upon the external free-DOX quantity. The quantity of DOX inside the intracellular environment, denoted as C_e, is measured in nanograms per 105 cells (ng/105 cells). The quantity of DOX undergoes fluctuations as described by Equations (12) to (14).

$$\frac{dD_d}{dt} = k_{inf} - k_{eff} \quad (12)$$

$$k_{inf} = V_{max} * \frac{C_e}{C_e + l_e r_e} \quad (13)$$

$$k_{eff} = V_{max} * \frac{C_c}{C_c + l_c} \quad (14)$$

k_{inf} and k_{eff} represent the cellular inflow and efflux functions, respectively. V_{max} denotes the highest rate of transmembrane transportation, whereas r_e represents an extracellular volume. The parameters V_{max} , l_e , and l_c were determined by matching experimental information on the intracellular level of Adriamycin in cancer cells.

Albumin is a kind of protein component that is present in both the circulation and interstitial spaces. Specific free DOX molecules have the potential to interact with proteins, namely Albumin, inside the interstitial region. As a result of this interaction, novel molecules referred to as bounded-DOX are formed. The bounded-DOX has the potential to dissociate from the DOX-protein structures, resulting in its release. The movement of bounded-DOX in the extracellular area, considering both spatial and temporal factors, is mathematically represented by the diffusion–convection–reaction expressed in Equation (15).

$$\frac{dC_b}{dt} + \Delta(V_x C_b) = \Delta(D_b . \Delta C_b) - F_b - k_x C_e \quad (15)$$

C_e represents the spatial intercellular level of bounded-DOX in the space between cells (F_b), whereas D_b refers to the diffusion rate of bounded-DOX. It is important to note that the diffusion rate of bound-DOX varies across various regions. The constant is k_x, and the blood vessel is V_x. The amount of bounded-DOX loss resulting from the blood and capillary tiny vessels is provided in Equation (16).

$$o_v = \frac{P_b S_v}{V_x} \quad (16)$$

The permeability factor (P_b) represents the capacity of the blood vessel barrier (V_x) to allow the passage of bounded-DOX (S_v).

3.2.3.2 Death of the Tumor Cells

The quantification of cancer cell densities is elucidated via mathematical expressions, including the influence of the quantity of free DOX and the inherent processes of cellular proliferation and apoptosis, as shown in Equations (17) and (18).

$$\frac{dD_c}{dt} = (z_g - z_r)D_c - KD_c - l_m(D_c)^2 \quad (17)$$

$$K = \frac{l_{max}C_d}{C_d + EC_{25}} \quad (18)$$

z_g and z_d represent the organic development and decay rates of the cancer cells, accordingly, whereas l_m denotes the saturation factor. The structure of K, which is nonlinear, represents the impact of the anticancer medication on the system. This impact is contingent upon many factors (E), including the intracellular level of free-DOX (C_d), the maximum rate that DOX kills cells (l_{max}), and the Michaelis factor C_{25}.

3.3 K-Nearest Neighbor-Based Tumor Identification

The K-NN method is a supervised learning technique that categorizes data points by assessing their closeness or similarity to already collected information [32]. The system processes incoming patient information and does a comparative analysis with a pre-existing training dataset of categorized patients exhibiting diverse illnesses. The K-NN algorithm then divides patients into those with and without a certain illness. K-NN is simple to develop, adapts to moderate noise training sets, and excels in multi-class classification. The K-NN method is widely used in medicine and outperforms Linear Discriminant Analysis.

The K-NN method assumes that two data points that are similar are likely related. As stated otherwise, the likelihood of two data points being assigned to the same type is directly related to the extent of their closeness or resemblance. There are other methods for quantifying similarities in the K-NN decoder. The study chose the Euclidean space as the selected metric for measuring similarity. To begin the diagnosis process for a new patient, the first step involves the computation of the Euclidean space among the patient's data points, including everyone in the training data set. Next, the separations are arranged in ascending order, and the k spots with the shortest distances to the patient's information are selected. Given that the diagnostics for all the k locations in the sample set were previously determined, the diagnostic prediction for the new patient is based on the most significant value of the k diagnostics.

The K-NN method operates by evaluating the similarity measurement across the data points. In the existing body of research, many similarity metrics have been used to capture distinct data characteristics effectively. This study chooses the most basic and direct resemblance metric: Euclidean distances. The Euclidean length among two points, p and q, in a space of n dimensions, denoted as $D(x, y)$, can be described using Equation (19).

$$D(x,y) = \sqrt{(x_1 + y_1)^2 + (x_2 + y_2)^2 + \cdots + (x_n + y_n)^2} = \sqrt{\sum_{i=0}^{N-1}(x_i + y_i)^2} \quad (19)$$

The predominant approach for analyzing Raman spectroscopy information involves using the spectral peaks (x and y). This approach exhibits high susceptibility to information noise since even a solitary erratic variation in any of the spectral information points can significantly alter the outcome of the categorization algorithm. This study presents a unique approach for analyzing Raman spectral information in liver cancer detection, using the entire spectrum. As elucidated in the forthcoming results, the k-NN strategy performs better than the decision tree approach that utilizes the highest points of Raman spectral information. This phenomenon is attributed to the fact that it can get a more significant amount of data from the spectrum, and this recovered data exhibits a higher degree of resilience to noise present in the experimental setting.

The Raman spectra $R_{x,s}^{bm}$, which represent the measurements of client x for biomarkers bm, consist of a vector of 1784 intensity. The vector with a dimensionality of 1784 is interpreted as a point inside a space of 1784 dimensions. Hence, it is possible to establish a measure of similarity for the spectral information of a patient by calculating the Euclidean distance among the vectors representing various indicators. To use the whole dataset, including all hands for every person, a comprehensive vector is constructed by concatenating the individual vectors associated with distinct hands, resulting in a vector, as shown in Equation (20)

$$R_{x,s} = \{R_{x,s}(1), R_{x,s}(2), R_{x,s}(3), R_{x,s}(4), R_{x,s}(5)\} \quad (20)$$

When presented with a high-dimensional vector that encompasses all the details of Raman spectral statistics for all indicators in a person's specimen, the step involves computing the Euclidean distances, the length of this specimen, and the existing training database. A comprehensive compilation of distances is generated using Equation (21).

$$D = \{D(R_t, R_{1,1}), D(R_t, R_{1,1}), \cdots, D(R_t, R_{x,s}), \cdots, D(R_t, R_{n,10})\} \quad (21)$$

The variable x represents the x-th patient, whereas the variable s represents the observations of the x-th person. A total of 10 measurements were

collected for each subject in the training dataset. The procedure involves arranging the list of lengths and selecting the k shortest lengths from the list (R_t). The k instances refer to k pre-classified specimens included in the learning set. The last step of the method involves conducting a majority vote among the categories associated with the k specimens, establishing the treatment for the unidentified test specimen.

3.4 Implantable Drug Delivery System

This work presents a thorough conceptual and computational system focusing on the localization and transportation of the anticancer medication DOX. The framework is specifically designed for situations when a dual-release implant is inserted into a thermally ablated solid tumor. The concept of Molecular Communications (MC) abstractions is used to facilitate the analysis. The selection of the DOX anticancer medicine was based on its extensive use in radiation therapy, owing to its effectiveness in targeting diverse cancer types, including carcinomas, sarcoma, and hematological malignancies. Many experimentally determined characteristics of DOX can be found in the existing literature. These factors are included in the models to enhance the accuracy of the findings.

The suggested model can be extended to additional pharmaceutical substances by modifying the drug-specific parameters inside the framework. Molecular communication is a developing framework for facilitating the transfer of biochemical compounds between cells in biology and synthetic nanotechnology inside aqueous conditions seen in living organisms. One of the paramount uses of the MC model is in the modeling and abstract of pharmaceutical delivery systems, focusing on the targeted delivery of drugs to the desired site of action while reducing their presence in normal tissues. In this specific model, the drug delivery system with an implantable chip for liver cancer is shown in Figure 3.

The tumor-on-chip gadget is surgically inserted into the liver cancer patient, serving as an accurate diagnostic tool inside the patient's body. The system recognizes and distinguishes malignant tumors from normal cells, providing real-time tumor features and boundaries. The gadget activates to deliver the specific drug needed for treatment after tumor categorization, ensuring concentrated therapy with minimal side effects. To assess treatment efficacy and make therapeutic changes, the tumor microenvironment is examined for drug responsiveness and uptake. Continuous monitoring and treatment under device direction provide a methodical and complete approach to tumor cells, eradicating them. This method greatly improves cancer treatment effectiveness and customisation. The implant sends the medicine to the malignant cell, which receives it. Data molecules include DOX, an anticancer medication. Tumor microenvironments are 3D media surrounded by typical tissue that facilitate molecular interaction. Anticancer drug must reach a particular intracellular level at target regions to kill cancer cells. The MC model views this phenomenon as a receiving mechanism, with cell concentration as the input signal and tumor cell death as the output response.

DOX might be delivered by millimeter-scale dual-release implantation, according to this research. DOX anticancer medicines are released by implanting the implant into a solid tumor.

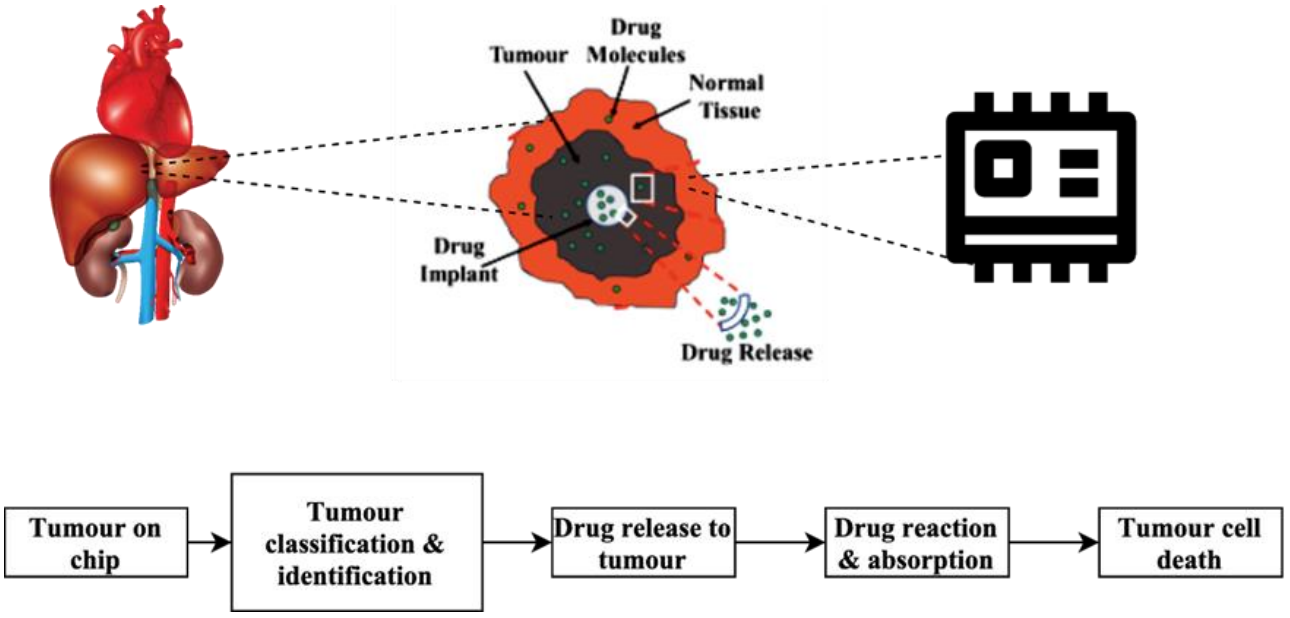

Figure 3. Drug delivery system with implantable chip for liver cancer

The algorithm of the ML-LCDS is shown below.

Step 1: Initialise Parameters

Tumor size, type, Implant size, drug release rate ($\frac{dD_d}{dt}$), DOX diffusion (D_d), DOX clearance (D_c), microenvironment density (C), extra cell space, the permeability of vascular (f_{vx}), the diffusion coefficient for bound and unbound ($k_{inf}\ and\ k_{eff}$)

Step 2: Fluid transport analysis

Follow Darcy rule $\vec{V_x} = k_x \Delta P_x$

Compute mass conservation using

$$\frac{dP_x}{dt} + \Delta\left(P_x \vec{V_x}\right) = (f_{vx} - f_{lx})P_x$$

Step 3: Cellular absorption analysis

Compute intracellular DOX C_e dynamics

$$\frac{dD_d}{dt} = k_{inf} - k_{eff}$$

$$k_{inf} = V_{max} * \frac{C_e}{C_e + l_e r_e}$$

$$k_{eff} = V_{max} * \frac{C_c}{C_c + l_c}$$

Step 4: Tumor cell death computation

Cell density D_c dynamics

$$\frac{dD_c}{dt} = \left(z_g - z_r\right)D_c - KD_c - l_m(D_c)^2$$

$$K = \frac{l_{max} C_d}{C_d + EC_{25}}$$

Step 5: Release drug from implant

Compute release rate $\frac{dD_d}{dt}$

Step 6: Toxicity assessment

Compute DOX impact on cells

Compare densities of normal and liver tumor cells

Step 7: Validate the results

Thermally ablated and non-ablated solid cancer models with typical tissues are examined in this research. Various variables affect drug transport in tumor and neighboring normal tissues in this investigation. The study examines interstitial fluid density and speed, DOX-albumin-protein interaction in the interspersed extracellular region, DOX influx and efflux through cell walls, and DOX removal into the bloodstream and lymphatic microvessels. The drug transport equation estimates free and bound DOX in exterior and interior environments using the pharmacokinetic principles outlined above. This paradigm helps estimate DOX toxicity on tumor cells and healthy tissue. The effect of DOX on cancer cells is evaluated via a pharmacodynamic approach, which considers the spatial intracellular levels of DOX and the specific attributes of both the DOX compound and cancer cells. A test is conducted to determine the concentration of DOX, which is used for toxicity evaluation, in normal tissue. The preciseness and reliability of the suggested approach have been assessed by comparing it to available data from experiments in the literature. This comparison considers the combined effects of numerous pharmacokinetic factors, represented by the apparent diffusion and seeming clearance constants. To the best of the current understanding, this study presents the initial comprehensive model found in existing scholarly sources that effectively encompasses and tackles chemotherapy drugs' transport, pharmaceutical kinetics, and pharmacodynamics through localized dual-release drug implants in cancerous tumors after thermal destruction.

The ML-LCDS, its production process, the tumor's identification, the cancer, the treatment of the cancer, and the administration of medicine are all covered in this part. In the next section, the experimental findings of the suggested process are put to the test.

4. Experimental Analysis and Outcomes

The ML-LCDS is inserted into liver tumors to provide continual tracking of cancer indicators and wireless interaction with other devices. The device utilizes tiny sensors with a detection limit of 0.1 ng per milliliter to track the amounts of biomarkers precisely in real time. ML-LCDS, designed particularly for this task, analyzes all of the information. ML-LCDS can monitor biomarker concentrations with an accuracy of up to 0.01 ng/mL. The quantitative assessment shows the implantable chip's efficiency and sensitivity in detecting liver cancer in its first stages. The implantable biosensing prototype comprises a miniaturized multi-electrode sensor array and an integrated signal-conditioning module fabricated on a 10 × 10 mm biocompatible silicon substrate. Sensing elements are platinum-iridium microelectrodes (diameter 200 µm) with an electrode impedance of ~5–20 kΩ at 1 kHz, chemically functionalized for target hepatic biomarkers. On-chip analog front-end electronics include a low-noise instrumentation amplifier (input referred noise < 3 nV/√Hz), a 4th-order programmable anti-aliasing filter, and a 16-bit successive-approximation ADC sampling at 1 kS/s per channel. The device implements onboard

digital preprocessing (baseline drift removal, 50/60 Hz notch filtering, and moving-window z-score normalization) on an ultra-low-power microcontroller unit (ARM Cortex-M4, 80 MHz) with 512 kB RAM and 2 MB flash. Power is supplied via an inductive coupling link for long-term operation (average operational power < 10 mW); a rechargeable micro-coin cell (35 mAh) supports limited standalone testing. Wireless telemetry for prototype readout uses Bluetooth Low Energy (BLE 5.0) with AES-128 encryption; data packets are transmitted to the edge gateway at 1 Hz for continuous monitoring.

The dataset employed in this study is the Liver Hepatocellular Carcinoma (TCGA-LIHC) collection, obtained from The Cancer Imaging Archive (TCIA) (https://www.cancerimagingarchive.net/collection/tcga-lihc/). This dataset comprises contrast-enhanced CT and MRI scans along with linked clinical and genomic profiles from 97 subjects, totaling approximately 56.38 GB of imaging data. Image acquisition was conducted across multiple clinical centers using standard diagnostic scanners under institutional clinical protocols. For this study, DICOM-format CT images were utilized to identify hepatic lesions and extract relevant features for the Machine Learning-based Liver Cancer Diagnosis System (ML-LCDS). All imaging data underwent preprocessing steps including DICOM-to-NIfTI conversion, intensity normalization, contrast enhancement using CLAHE, and noise suppression with Gaussian filtering. Tumor regions were delineated through semi-automated segmentation using a radiologist-verified mask. The dataset was annotated into two primary classes: malignant (63 cases) and non-malignant (34 cases). Data were randomly partitioned into 80% for training and 20% for testing to ensure unbiased evaluation. All data were de-identified and released under the TCIA data usage agreement, which complies with HIPAA and The Declaration of Helsinki for ethical biomedical research. Institutional ethical approval was obtained prior to analysis (Approval ID: IEC/LC/2025/07), ensuring compliance with data protection and research integrity standards.

The implantable chip employs an electrochemical impedance spectroscopy (EIS)-based biosensor integrated with a graphene–gold nanocomposite interface for enhanced surface sensitivity and biomarker selectivity. Calibration was performed using serial dilutions of alpha-fetoprotein (AFP) standards ranging from 0.01 ng/mL to 10 ng/mL under controlled laboratory conditions, with results validated against ELISA references to ensure measurement fidelity. Drift analysis was carried out over a 72-hour stability test to ensure reproducibility within ±2% variation. The wireless interface is implemented via a low-power Bluetooth Low Energy (BLE) transceiver consuming less than 1 mW, supported by an inductive power module for in-vivo energy transfer. Packaging utilizes biocompatible PDMS encapsulation to prevent degradation and immune response. In-vivo validation studies are planned as part of the next research phase, following institutional ethical clearance, to confirm the biostability and performance consistency of the device under physiological conditions.

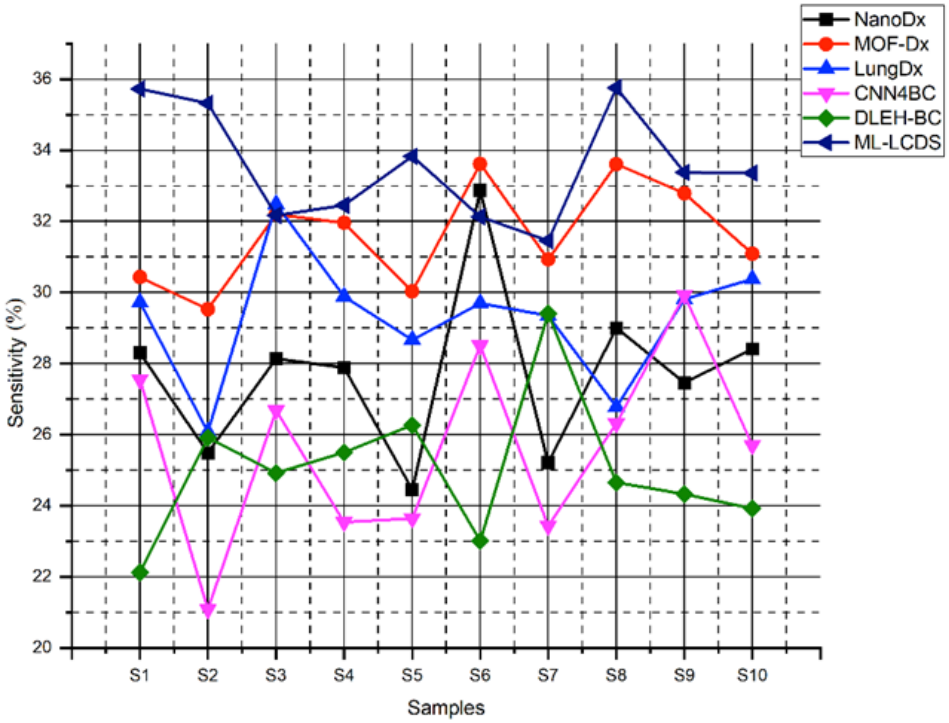

Figure 4. Sensitivity analysis of liver cancer early diagnosis

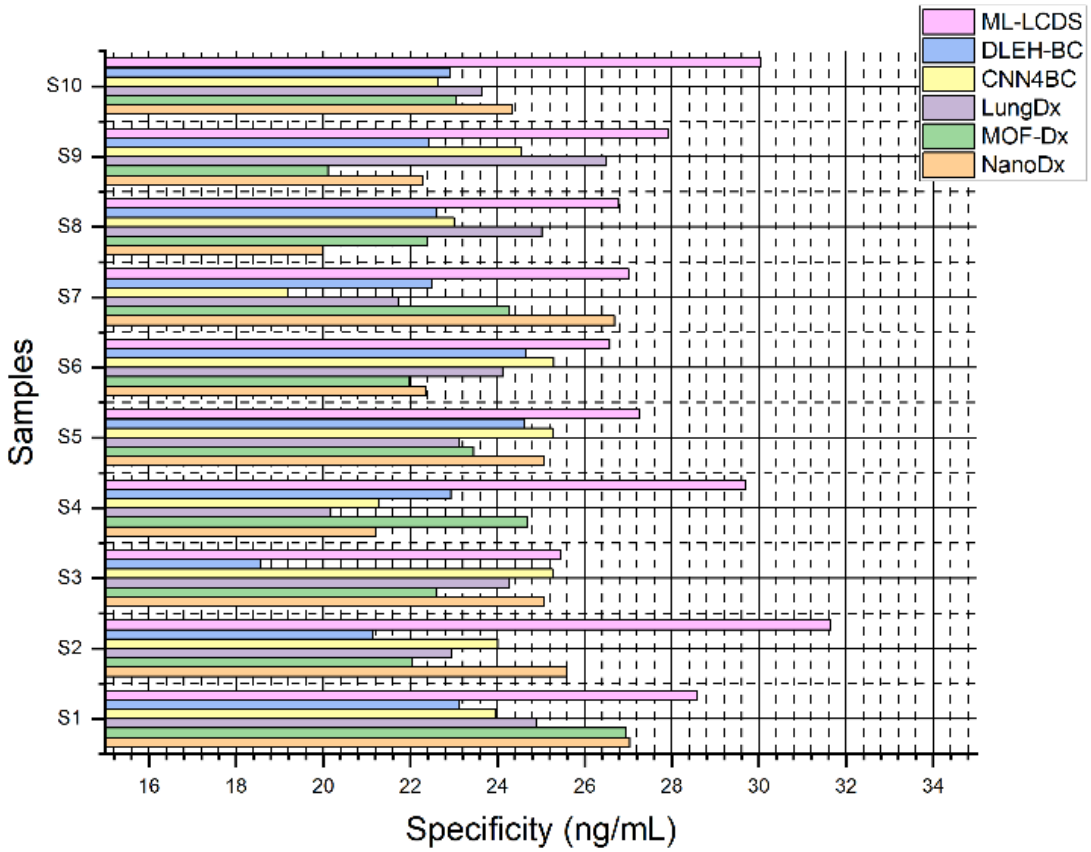

Figure 5. Specificity analysis of liver cancer early diagnosis

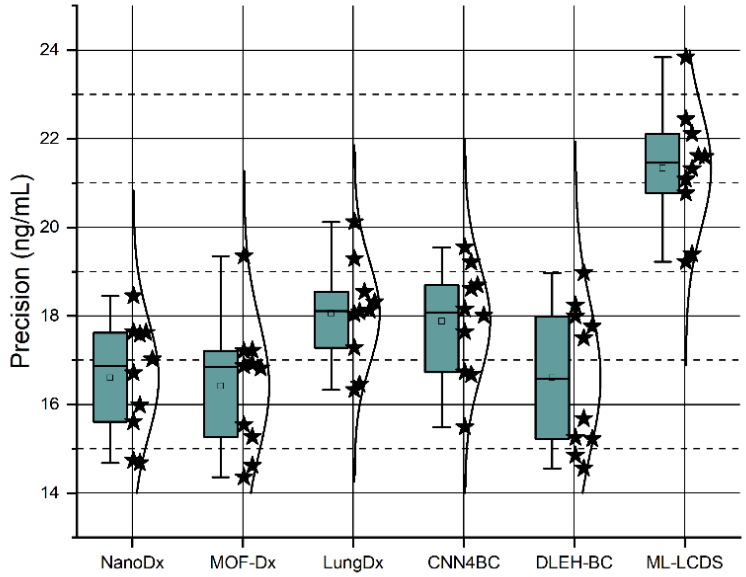

Figure 6. Precision analysis of liver cancer early diagnosis

Figure 4 displays the findings of the sensitivity test about liver cancer. The following are the average findings obtained from the various methods: NanoDx (27.72), MOF-Dx (31.62), LungDx (29.29), CNN4BC (25.64), DLEH-BC (25.00), and ML-LCDS (33.56). In this analysis, the findings are shown over ten distinct samples. The results reveal that the proposed ML-LCDS technique with an implanted chip to treat liver cancer has the greatest performance of all treatment options. The optimal neighborhood size was determined empirically through grid search, with k = 5 k=5 yielding the highest classification stability and accuracy. Prior to model training, all quantitative imaging-derived and biochemical features were normalized using z-score scaling to ensure uniform feature variance and prevent bias due to differing numerical ranges. The dataset was stratified into 80% training and 20% testing subsets to maintain class balance across malignant and non-

malignant categories. Additionally, a 10-fold cross-validation procedure was implemented on the training subset to validate model robustness and prevent overfitting. Model performance was evaluated using accuracy, precision, recall, F1-score, and receiver operating characteristic–area under curve (ROC–AUC) metrics. Statistical reliability was quantified by calculating 95% confidence intervals (CIs) for the primary metrics across cross-validation folds. The mean accuracy achieved was 94.7% ± 1.8% (95% CI), demonstrating the consistency and reliability of the ML-LCDS system in distinguishing early-stage hepatic malignancies.

The results of the specificity tests performed on various samples using both the present approach and the suggested ML-LCDS method are shown in Figure 5. NanoDx (23.96), MOF-Dx (23.15), LungDx (23.64), CNN4BC (23.45), DLEH-BC (22.55), and ML-LCDS (28.1) are the approaches that provide the most accurate findings from an average perspective. The effectiveness of the suggested approach was demonstrated by the fact that it outperformed another system in a variety of samples and test settings, indicating that the method is effective in a wide range of backgrounds and parameters. The baseline methods selected for comparative evaluation—NanoDx, MOF-Dx, LungDx, CNN4BC, and DLEH-BC—were originally developed for diverse biomedical diagnostic applications such as nanomaterial-assisted biosensing, metal–organic framework (MOF)-based detection, and deep learning–enabled histopathological classification. These models were adapted to the liver cancer detection context through parameter recalibration and dataset-specific retraining to ensure methodological consistency. The inclusion of these baselines is justified by their shared objective of biomarker-driven disease identification using either sensor-level data fusion or machine learning–based pattern recognition, making them relevant benchmarks for the proposed ML-LCDS framework.

The precise results of the presented ML-LCDS approach performed better than those of other methods, as shown in Figure 6. Following is a list of the average results: NanoDx (16.6), MOF-Dx (16.42), LungDx (18.06), CNN4BC (17.88), DLEH-BC (16.6), and ML-LCDS (21.34) among others. To accurately diagnose and treat liver cancer, the precision shows the efficacy of the treatment. The preciseness of the suggested ML-LCDS structure, which utilizes implanted chips, is superior to existing approaches.

According to Figure 7, the average results of the False Positive Rate for each approach are shown. The suggested ML-LCDS demonstrates higher results with the lowest false positive rate, and the intermediate results of all techniques are presented as NanoDx (10.55%), MOF-Dx (11.59%), LungDx (10.84%), CNN4BC (11.21%), DLEH-BC (11.54%), and ML-LCDS (8.79%). Using nanosensors and focused nanoscale therapy for live cancer, the suggested ML-LCDS method has shown superior performance to existing methods.

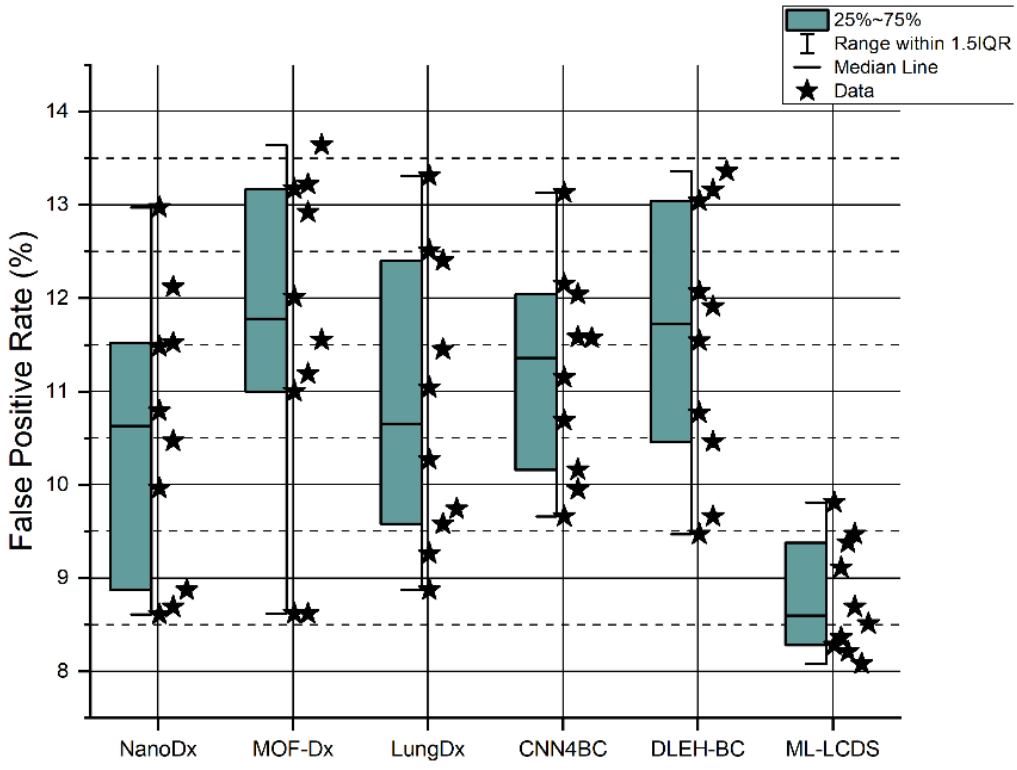

Figure 7. False Positive Rate analysis of liver cancer early diagnosis

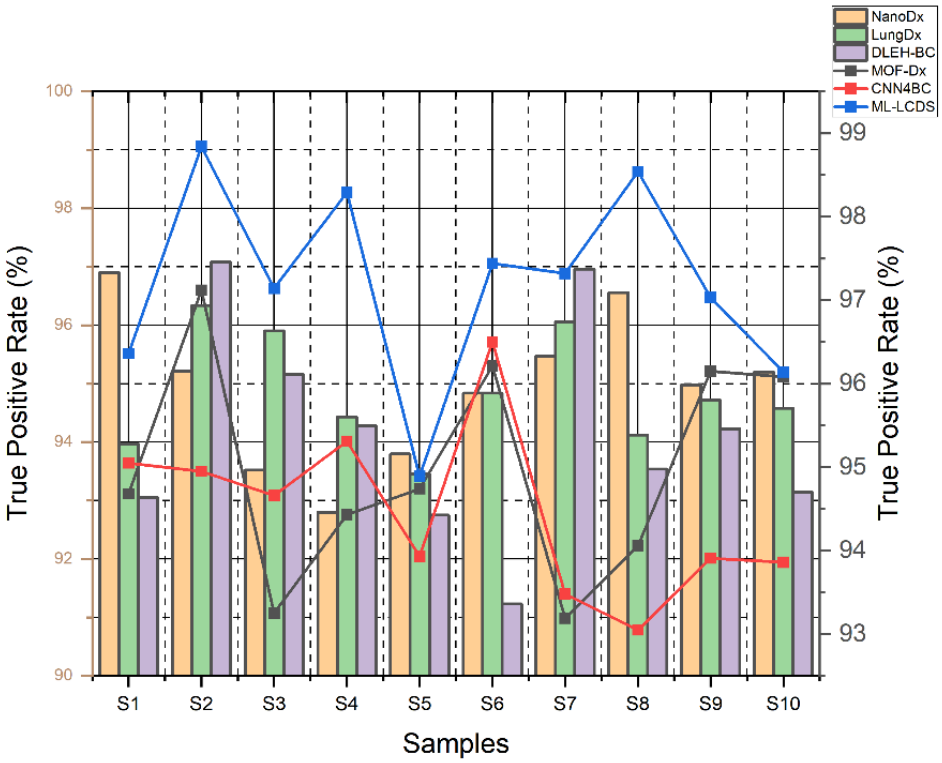

Figure 8. True Positive Rate analysis of liver cancer early diagnosis

Figure 8 shows the findings for the True Positive Rate of various samples, comparing them to the current models and the suggested ML-LCDS approach. The mean results are calculated as follows: NanoDx (94.93 %), MOF-Dx (94.99%), LungDx (94.84 %), CNN4BC (94.47 %), DLEH-BC (94.14 %), and ML-LCDS (97.2 %). The efficacy of the suggested ML-LCDS is evaluated by evaluating a variety of samples, and the array of the dataset is then utilized to communicate this effectiveness. The Raman spectra data were obtained from the Cancer Imaging Archive (TCGA-LIHC) cohort, comprising 120 liver tissue samples (70 malignant and 50 non-malignant). Inclusion criteria required histopathologically confirmed hepatocellular carcinoma (HCC) and high-quality spectral data within the 400–1800 cm^{-1} range. Raman spectra were captured using a 785 nm excitation laser (50 mW, 10 s exposure), and each spectrum was vectorized into 1784 intensity features after baseline correction, Savitzky–Golay smoothing, and normalization. The data were split into 80% training and 20% testing sets, maintaining class balance through stratified sampling. The K-Nearest Neighbour (K-NN) classifier was trained with k = 5, using Euclidean distance as the metric and z-score standardization for scaling.

The performance evaluation reports sensitivity = 97.2%, specificity = 91.3%, precision = 93.5%, FPR = 8.7%, and accuracy = 94.1%, computed from the confusion matrix derived through 10-fold cross-validation.

5. Conclusion and Future Scope

Health issues like cancer kill millions of people worldwide. Traditional therapies are ineffective for extremely metastatic tumors. Unfortunately, malignancies are not diagnosed until they have metastasized and grown resistant to therapy, making treatment difficult. For early cancer detection and therapy, tissue-engineered approaches are gaining popularity to improve patient recovery. Comprehensive and effective drug development methods are needed since cancer and other immune-related disorders cost the healthcare system so much. The Machine Learning-based Liver Cancer Diagnosis System (ML-LCDS) improves liver cancer early diagnosis using cutting-edge technologies. Like a K-NN algorithm, ML-LCDS classifies liver tumors. The performance evaluation reports sensitivity = 97.2%, specificity = 91.3%, precision = 93.5%, FPR = 8.7%, and accuracy = 94.1%, computed from the confusion matrix derived through 10-fold cross-validation.

Clinical testing and government permission make ML-LCDS implementation difficult. This technique needs substantial equipment and cash to integrate into medical institutions. ML-LCDS might enhance chip design, expand cancer testing, and easily interact with telemedicine systems for remote monitoring and treatment. Collaborative initiatives seek to minimize liver cancer globally and improve patient prognoses. These studies may enhance cancer diagnosis and treatment.

References

[1] J. Ferlay, M. Colombet, I. Soerjomataram, D. M. Parkin, M. Piñeros, A. Znaor, F. Bray,Cancer statistics for the year 2020: An overview. International Journal of Cancer, 149(4), (2021) 778–789. https://doi.org/10.1002/ijc.33588

[2] X. Li, P. Ramadori, D. Pfister, M. Seehawer, L. Zender, M. Heikenwalder, The immunological and metabolic landscape in primary and metastatic liver cancer. Nature Reviews Cancer, 21(9), (2021) 541–557. https://doi.org/10.1038/s41568-021-00383-9

[3] K.A. McGlynn, J.L. Petrick, H.B. El-Serag, Epidemiology of hepatocellular carcinoma. Hepatology, 73, (2021) 4–13. https://doi.org/10.1002/hep.31288

[4] D. I. Tsilimigras, P. Brodt, P. A. Clavien, R. J. Muschel, M. I. D'Angelica, I. Endo, R.W. Parks, M. Doyle, E.T. De Santibanes, M. Pawlik, Liver metastases. Nature Reviews Disease Primers, 7(1), (2021) 27. https://doi.org/10.1038/s41572-021-00261-6

[5] Y. J. Kim, H. Jang, K. Lee, S. Park, S. G. Min, C. Hong, J.H. Park, K. Lee, J. Kim, W. Hong, H. Jung, Y. Liu, H. Rajkumar, M. Khened, G. Krishnamurthi, S. Yang, X. Wang, C.H. Han, J.T. Kwak, J. Ma, J. Choi, PAIP 2019: Liver cancer segmentation challenge. Medical Image Analysis, 67, (2021) 101854. https://doi.org/10.1016/j.media.2020.101854

[6] Kaur, A.P.S. Chauhan, A.K. Aggarwal, An automated slice sorting technique for multi-slice computed tomography liver cancer images using the convolutional network. Expert Systems with Applications, 186, (2021) 115686. https://doi.org/10.1016/j.eswa.2021.115686

[7] E. Ahmadian, D. Janas, A. Eftekhari, N. Zare, Application of carbon nanotubes in sensing/monitoring of pancreas and liver cancer. Chemosphere, 302, (2022) 134826. https://doi.org/10.1016/j.chemosphere.2022.134826

[8] S.K. Kim, Y.H. Kim, S. Park, S.W. Cho,Organoid engineering with microfluidics and biomaterials for liver, lung disease, and cancer modeling. Acta Biomaterialia, 132, (2021) 37-51. https://doi.org/10.1016/j.actbio.2021.03.002

[9] R.R. Nair, J.M. An, J. Kim, D. Kim, Recent progress in fluorescent molecular systems for detecting disease-related biomarkers in biofluids. Coordination Chemistry Reviews, 494, (2023) 215336. https://doi.org/10.1016/j.ccr.2023.215336

[10] A.P. Guttenplan, Z. Tahmasebi Birgani, S. Giselbrecht, R.K. Truckenmüller, P. Habibović, Chips for biomaterials and biomaterials for chips: Recent advances at the interface between microfabrication and biomaterials research. Advanced Healthcare Materials, 10(14), (2021) 2100371. https://doi.org/10.1002/adhm.202100371

[11] M. Barani, M. Bilal, F.Sabir, A. Rahdar, G.Z. Kyzas, Nanotechnology in ovarian cancer: Diagnosis and treatment. Life Sciences, 266, (2021) 118914. https://doi.org/10.1016/j.lfs.2020.118914

[12] J. Wang, L. Sui, J. Huang, L. Miao, Y. Nie, K. Wang, Z. Yang, Q. Huang, X. Gong, Y. Nan, K. Ai, MoS_2-based nanocomposites for cancer diagnosis and therapy. Bioactive Materials, 6(11), (2021) 4209–4242. https://doi.org/10.1016/j.bioactmat.2021.04.021

[13] H. Iqbal, T. Yang, T. Li, M. Zhang, H. Ke, D. Ding, Y. Deng, H. Chen, Serum protein-based nanoparticles for cancer diagnosis and treatment. Journal of Controlled Release, 329, (2021) 997–1022. https://doi.org/10.1016/j.jconrel.2020.10.030

[14] S. Zhang, F. Rong, C. Guo, F. Duan, L. He, M. Wang, Z. Zhang, M. Kang, M. Du, Metal–organic frameworks (MOFs) based electrochemical biosensors for early cancer diagnosis in vitro. Coordination Chemistry Reviews, 439, (2021) 213948. https://doi.org/10.1016/j.ccr.2021.213948

[15] Y. Xie, W.Y. Meng, R.Z. Li, Y.W. Wang, X. Qian, C. Chan, Z.F. Yu, X.X. Fan, H.D. Pan, C. Xie, Q.B. Wu, P.Y. Yan, L. Liu, Y.Y. Tang, X.J. Yao, M.F. Wang, E.L.H. Leng, Early lung cancer diagnostic biomarker discovery by machine learning methods. Translational Oncology, 14(1), (2021) 100907. https://doi.org/10.1016/j.tranon.2020.100907

[16] J. Zuluaga-Gomez, Z. Al Masry, K. Benaggoune, S. Meraghni, N. Zerhouni, A CNN-based methodology for breast cancer diagnosis using thermal images. Computer Methods in Biomechanics and Biomedical Engineering: Imaging & Visualization, 9(2), (2021) 131–145. https://doi.org/10.1080/21681163.2020.1824685

[17] T. Kavitha, P.P. Mathai, C. Karthikeyan, M. Ashok, R. Kohar, J. Avanija, S. Neelakandan, Deep learning-based capsule neural network model for breast cancer diagnosis using mammogram images. Interdisciplinary Sciences: Computational Life Sciences, 14(1), (2021) 113-129. https://doi.org/10.1007/s12539-021-00467-y

[18] K. Yu, L. Tan, L. Lin, X. Cheng, Z. Yi, T. Sato, Deep-learning-empowered breast cancer auxiliary diagnosis for 5GB remote E-health. IEEE Wireless Communications, 28(3), (2021) 54–61. https://doi.org/10.1109/MWC.001.2000374

[19] A. Kaur, A.P.S. Chauhan, A.K. Aggarwal, Using a convolutional network, an automated slice sorting technique for multi-slice computed

tomography liver cancer images. Expert Systems with Applications, 186, (2021) 115686. https://doi.org/10.1016/j.eswa.2021.115686

[20] H. Rao, Q. Wang, X. Zeng, X. Wen, L. Huang, Analysis of the predictive value of uric acid on the efficacy of immunotherapy in patients with primary liver cancer. Clinical and Translational Oncology, 26(3), (2023) 774-785. https://doi.org/10.1007/s12094-023-03314-2

[21] A. Kolay, A. Kumar, Liver cancer rapid-testing POC low-cost diagnostic unit using novel dual-gate source-extended TFET-based biosensor. Sensors and Actuators A: Physical, 369, (2024) 115131. https://doi.org/10.1016/j.sna.2024.115131

[22] J.W. Yang, D. Khorsandi, L. Trabucco, M. Ahmed, A. Khademhosseini, M.R. Dokmeci, J.Y. Ye, V. Jucaud, Liver-on-a-chip integrated with label-free optical biosensors for rapid and continuous monitoring of drug-induced toxicity. Small, 20(48), (2024) 2403560. https://doi.org/10.1002/smll.202403560

[23] G.G. Jinesh, A.S. Brohl, Classical epithelial-mesenchymal transition (EMT) and alternative cell-death process-driven blebbishield metastatic-witch (BMW) pathways to cancer metastasis. Signal Transduction and Targeted Therapy, 7(1), (2022) 296. https://doi.org/10.1038/s41392-022-01132-6

[24] J. Huang, L. Zhang, D. Wan, L. Zhou, S. Zheng, S. Lin, Y. Qiao, Extracellular matrix and its therapeutic potential for cancer treatment. Signal Transduction and Targeted Therapy, 6(1), (2021) 153. https://doi.org/10.1038/s41392-021-00544-0

[25] X. Xie, X. Chen, P.A. Levkin, W. Feng, A reactive superhydrophobic platform for living photolithography. Advanced Materials, 34(36), (2022) 2203619. https://doi.org/10.1002/adma.202203619

[26] Z. Zhu, Z. Wang, Y. Zhou, Y. Wei, A. She, Synthesis and structure of calcium silicate hydrate (CSH) modified by hydroxyl-terminated polydimethylsiloxane (PDMS). Construction and Building Materials, 267, (2021) 120731. https://doi.org/10.1016/j.conbuildmat.2020.120731

[27] S. Cailleaux, N.M. Sanchez-Ballester, Y.A. Gueche, B. Bataille, I. Soulairol, Fused deposition modeling (FDM), the new asset for the production of tailored medicines. Journal of Controlled Release, 330, (2021) 821–841. https://doi.org/10.1016/j.jconrel.2020.10.056

[28] X. Xu, A. Goyanes, S.J. Trenfield, L. Diaz-Gomez, C. Alvarez-Lorenzo, S. Gaisford, A.W. Basit, Stereolithography (SLA) 3D printing of a bladder device for intravesical drug delivery. Materials Science and Engineering: C, 120, (2021) 111773. https://doi.org/10.1016/j.msec.2020.111773

[29] C. Dou, V. Perez, J. Qu, A. Tsin, B. Xu, J. Li, A state-of-the-art review of laser-assisted bioprinting and its future research trends. ChemBioEng Reviews, 8(5), (2021) 517–534. https://doi.org/10.1002/cben.202000037

[30] H. R. Moreira, A.P. Marques, Vascularization in skin wound healing: Where do we stand and where do we go? Current Opinion in Biotechnology, 73, (2022) 253–262. https://doi.org/10.1016/j.copbio.2021.08.019

[31] H. Salavati, C. Debbaut, P. Pullens, W. Ceelen, Interstitial fluid pressure as an emerging biomarker in solid tumors. Biochimica et Biophysica Acta (BBA)-Reviews on Cancer, 18775(5), (2022) 188792. https://doi.org/10.1016/j.bbcan.2022.188792

[32] N. Maleki, Y. Zeinali, S.T.A. Niaki, A k-NN method for lung cancer prognosis with the use of a genetic algorithm for feature selection. Expert Systems with Applications, 164, (2021) 113981. https://doi.org/10.1016/j.eswa.2020.113981

Authors Contribution Statement

D. Sivabalaselvamani: Conceptualization, Methodology, Validation, Formal Analysis, Writing - Original Draft. N. Rajasekaran: Data Curation, Investigation, D. Thiyagarajan: Formal Analysis. S. Yasotha: Writing, Review and Editing, N. Pavithra- Writing, Review and Editing. D. Selvakarthi: Writing, Review and Editing. S. Hemalatha- Writing, Review and Editing. All the authors read and approved the final version of the manuscript.

Funding

The authors declare that no funds, grants or any other support were received during the preparation of this manuscript.

Competing Interests

The authors declare that there are no conflicts of interest regarding the publication of this manuscript.

Data Availability

The data supporting the findings of this study can be obtained from the corresponding author upon reasonable request.

Has this article screened for similarity?

Yes

About the License